The Astrophysical Journal, 922:236 (10pp), 2021 December 1 https://doi.org/10.3847/1538-4357/ac29c6

Discovery of a Protocluster Core Associated with an Enormous Lya Nebula at $z = 2.3$

Qiong Li[1,2,3], Ran Wang[2], Helmut Dannerbauer[4,5], Zheng Cai[6], Bjorn Emonts[7], Jason Xavier Prochaska[8,9], Fabrizio Arrigoni Battaia[10], Roberto Neri[11], Chengpeng Zhang[1,2], Xiaohui Fan[12], Shuowen Jin[4,5], Ilsang Yoon[7], and Shane Bechtel[13]

[1] Department of Astronomy, School of Physics, Peking University, Beijing 100871, People's Republic of China
[2] Kavli Institute for Astronomy and Astrophysics, Peking University, Beijing, 100871, People's Republic of China; rwangkiaa@pku.edu.cn
[3] Department of Astronomy, University of Michigan, 311 West Hall, 1085 S. University Ave., Ann Arbor, MI, 48109-1107, USA
[4] Instituto de Astrofisica de Canarias (IAC), E-38205 La Laguna, Tenerife, Spain
[5] Universidad de La Laguna, Dpto. Astrofisica, E-38206 La Laguna, Tenerife, Spain
[6] Department of Astronomy, Tsinghua University, Beijing 100084, People's Republic of China
[7] National Radio Astronomy Observatory, 520 Edgemont Road, Charlottesville, VA 22903, USA
[8] Department of Astronomy and Astrophysics, University of California, 1156 High Street, Santa Cruz, California 95064, USA
[9] University of California Observatories, Lick Observatory, 1156 High Street, Santa Cruz, California 95064, USA
[10] Max-Planck-Institut fur Astrophysik, Karl-Schwarzschild-Str 1, D-85748 Garching bei München, Germany
[11] Institut de Radioastronomie Millimétrique (IRAM), 300 rue de la piscine, F-38406 Saint-Martin-d'Hères, France
[12] University of Arizona (Steward Observatory), USA
[13] Department of Physics, University of California, Santa Barbara, CA 93106, USA
Received 2021 February 1; revised 2021 September 7; accepted 2021 September 21; published 2021 December 3

Abstract

The MAMMOTH-1 nebula at $z = 2.317$ is an enormous Lyα nebula (ELAN) extending to a ~440 kpc scale at the center of the extreme galaxy overdensity BOSS 1441. In this paper, we present observations of the CO(3 − 2) and 250 GHz dust-continuum emission from MAMMOTH-1 using the IRAM NOrthern Extended Millimeter Array. Our observations show that CO(3 − 2) emission in this ELAN has not extended widespread emission into the circum- and inter-galactic media. We also find a remarkable concentration of six massive galaxies in CO(3 − 2) emission in the central ~100 kpc region of the ELAN. Their velocity dispersions suggest a total halo mass of $M_{200c} \sim 10^{13.1} M_{\odot}$, marking a possible protocluster core associated with the ELAN. The peak position of the CO(3 − 2) line emission from the obscured AGN is consistent with the location of the intensity peak of MAMMOTH-1 in the rest-frame UV band. Its luminosity line ratio between the CO(3 − 2) and CO(1 − 0) $r_{3,1}$ is 0.61 ± 0.17. The other five galaxies have CO(3 − 2) luminosities in the range of (2.1–7.1) × 10^9 K km s^{-1} pc^2, with the star-formation rates derived from the 250 GHz continuum of (<36)–224 $M_{\odot}$ yr^{-1}. Follow-up spectroscopic observations will further confirm more member galaxies and improve the accuracy of the halo mass estimation.

Unified Astronomy Thesaurus concepts: Active galaxies (17); Galaxies (573); Observational cosmology (1146); High-redshift galaxy clusters (2007); Protoclusters (1297); Active galactic nuclei (16)

1. Introduction

Enormous Lyα nebulae (ELANe) are rare and bright ($SB_{Ly\alpha} > 10^{-17}$ erg s^{-1} cm^{-2} arcsec^{-2}) Lyα-emitting regions extending up to hundreds of kpcs (e.g., Cantalupo et al. 2014; Cai et al. 2017a, 2018; Arrigoni Battaia et al. 2018b; Cai et al. 2019). They host multiple active galactic nuclei (Hennawi et al. 2015; Arrigoni Battaia et al. 2018a) and reside in overdense environments as seen from the Lyα emitters (LAEs) around them (Hennawi et al. 2015; Cai et al. 2017b). A major question is how the star-formation or AGN activities are fueled and evolve within the ELANe. To answer this question, cold molecular gas was mapped in the fields of these ELANe (e.g., Wagg & Kanekar 2012; Yang et al. 2012, 2014; Ao et al. 2020; Decarli et al. 2021).

The ELAN around the Spiderweb Galaxy (~250 kpc) at $z = 2.2$ (Miley et al. 2006) revealed the first evidence for the existence of a cold molecular circumgalactic medium (CGM) of the ELANe in the distant universe by using the Australia Telescope Compact Array (Emonts et al. 2016). CO(1 − 0) observations show a massive (~70 kpc, $M_{H2} \sim 10^{11} M_{\odot}$) reservoir of gas in the CGM that cooled well beyond the temperature of Lyα-emitting gas ($T \sim 10^4$ K) and is actively feeding star formation across the halo. CO(4 − 3) and [C I] are detected across ~50 kpc, following the distribution of previously detected low-surface-brightness CO(1 − 0) across the CGM (Emonts et al. 2018). Its line ratio and carbon abundance are similar to that of the Milky Way and star-forming galaxies (SFGs) (Emonts et al. 2018). Thus, observations of the CO emission from the ELANe has the potential (i) to probe the physical conditions and kinematics of the cold gas component within the system and (ii) to constrain the energy and momentum output released by the star-formation and/or AGN activities into the interstellar/circumgalactic medium (ISM/CGM). Furthermore, such observations will address the nature of the central source and the mechanism that powers these gaseous nebulae.

The ELAN MAMMOTH-1 is an enormous Lyα nebula discovered by Cai et al. (2017a), extending to a 442 kpc scale. It is also the first radio-quiet source to have strongly extended (~30 kpc) [C IV] and [He II] emission (Cai et al. 2017a). MAMMOTH-1 resides in an extremely overdense field, BOSS1441, containing strong Lyα absorptions at $z = 2.32 \pm 0.02$ in the spectra of five background QSOs, projected within 20 h^{-1} Mpc scale (Cai et al. 2017b). Cai et al. (2017b) confirmed that the LAE overdensity ($\delta_{LAE} = \rho_{LAE}/\langle\rho_{LAE}\rangle - 1$) in the MAMMOTH-1 field is 10.8 ± 2.0 on 15 Mpc, which could be one of the most overdense fields found to date. Arrigoni Battaia et al. (2018b) also revealed

Table 1
IRAM NOEMA Measurements of The ELAN MAMMOTH-I

Source	R.A. J2000	Decl. J2000	redshift	Δv_{CO} km s^{-1}	FWHM$_{CO}$ km s^{-1}	$I_{CO(3-2)}$ Jy km s^{-1}	$S_{250\ GHz}$ mJy
(1)	(2)	(3)	(4)	(5)	(6)	(7)	(8)
G1(A)	14:41:24.72	+40:03:15.14	2.3088 ± 0.0004	−310	180 ± 30	0.298 ± 0.044	0.74 ± 0.15[a]
G2(B)	14:41:24.50	+40:03:09.90	2.3123 ± 0.0006	0	370 ± 90	0.237 ± 0.051	0.14 ± 0.03[b]
G3	14:41:24.75	+40:03:08.17	2.3137 ± 0.0004	120	180 ± 80	0.113 ± 0.040	<0.12
G4	14:41:23.95	+40:03:03.69	2.3059 ± 0.0004	−580	160 ± 50	0.182 ± 0.046	<0.12
G5	14:41:23.98	+40:03:12.66	2.3037 ± 0.0003	−770	80 ± 30	0.092 ± 0.030	<0.12
G6(C)	14:41:23.83	+40:03:08.00	2.3067 ± 0.0005	−500	280 ± 70	0.245 ± 0.056	0.18 ± 0.05

Notes. Col (1): Source name. Cols. (2) and (3): R.A. and decl. in J2000. Col. (4): spectroscopic redshift derived from the CO(3 − 2) observations. Col (5): the offset velocity of the CO(3 − 2) peak emission, respect to Source B. Col (6): the FWHM of CO(3 − 2), derived by a Gaussian fitting to the CO(3 − 2) profile. Col (7): CO(3 − 2) integrated velocity intensity. The intensity and luminosity errors are derived from the fitting of the emission-line profile of the CO peak. Col (8): 250 GHz dust-continuum observations, upper limits for G3, G4, and G5 are 3σ.

[a] G1 is marginally resolved at the 250 GHz continuum map along the major axis $(1.25 \pm 0.32)'' \times (0.57 \pm 0.26)''$. The continuum source position is 14:41:24.71 +40.03.15.13.

[b] A $> 4\sigma$ peak close to G2 (central AGN of MAMMOTH-I): The 250 GHz continuum peak position is 14:41:24.48 40:03:08.98, about 0.″7 away from the phase center.

an overdensity of submillimeter galaxies (SMGs) of $\delta_{SMG} = 3.0$ around the peak area of this LAE overdensity by using the Submillimetre Common-User Bolometer Array-2 (SCUBA-2) on the James Clerk Maxwell Telescope. Its oberved frame 350 GHz (850 μm) continuum detection suggests the far-infrared (FIR) luminosity of $L_{FIR} = 2.4 \times 10^{12} L_{\odot}$ from ELAN MAMMOTH-I by assuming a dust temperature of 45 K and an emissivity index of 1.6 (Arrigoni Battaia et al. 2018b). The optical, IR, and submillimeter observations of the ELAN MAMMOTH-1 suggest that this ELAN could be powered by an extreme system with massive star formation and strong AGN activity in the middle of a massive large-scale structure. Furthermore, Emonts et al. (2019) detected CO(1 − 0) luminosity of $L'_{CO(1-0)} \sim 3.8 \pm 0.8 \times 10^{10}$ K km s^{-1} pc^2 from the ELAN MAMMOTH-I, revealing a molecular gas mass of $M_{H2} \sim 1.4(\alpha_{CO}/3.6) \times 10^{11} M_{\odot}$. Strikingly, 50% of the CO(1 − 0) spans ∼30 kpc into the CGM.

In this work, we present IRAM NOrthern Extended Millimeter Array (NOEMA) observations of the CO(3 − 2) line and 250 GHz continuum emission. These provide us further information about the dense gas and star-forming activity in and around this ELAN. We describe the observations and data reduction in Section 2, and present the results in Section 3. Then we report the newly discovered galaxy group (a protocluster core) within this system and discuss the properties of the molecular gas from the galaxy members in Section 4. We conclude with a brief summary in Section 5. Throughout this paper, we assume a flat cosmological model with $\Omega_{\Lambda} = 0.7$, $\Omega_m = 0.3$, and $H_0 = 70$ km s^{-1} Mpc^{-1}. Finally, we note that based on the flux peak of the Lyα emission, Cai et al. (2017b) defined the center of the MAMMOTH-I Nebula as *Source B*. Follow-up studies of MAMMOTH-I (e.g., Emonts et al. 2019 and Arrigoni Battaia et al. 2018b) adopt its terminology. Here, we follow this naming convention; see also Tables 1 and 2.

2. NOEMA Observations

2.1. CO(3 − 2) Transition

The ELAN MAMMOTH-1 was observed with NOEMA (ID: S18CW) centered on $(\alpha_{2000}, \delta_{2000}) = (14^h41^m24^s.47, +40° 03' 09''.67)$ between 2018 November to 2019 January in C configuration with 10 antennas. The total observing time is 8 hr and the on-source time is 4.6 hr. We use the 3 mm receiver and the correlator PolyFix in dual polarization mode, tuning one of the 3.9 GHz basebands on the observed frequency 104.250 GHz of the redshifted CO(3 − 2) transition.

We use the quasars 1505+428, 1504+377, and J1438+371 as phase and amplitude calibrators. The RF calibrators were 2013+370 and 3C273, the flux calibrator was MWC349. In the 3 mm band (band 1 of NOEMA), the absolute flux calibration is accurate within 10%. The calibrated visibility data were imaged with the software package MAPPING (part of GILDAS), using natural baseline weighting and the Hogbom cleaning algorithm. The final synthesized beam sizes are $2''.3 \times 1''.6$. To further check if there are missing CO intensities in a more extended area, we tapered and re-weighted the visibilities to a lower angular resolution of $3''.2 \times 3''.2$. The field of view (primary beam) for NOEMA observations at $\nu_{obs} = 100$ GHz are 50″. Then we made the primary beam correction. The maximum recoverable scale at the observed frame 100 GHz is roughly 41″. The 1σ rms sensitivity of the natural-weighted image cube is 0.3 mJy beam^{-1} per 45 km s^{-1} channel, while the rms of the tapered-image cube is 0.4 mJy beam^{-1} per 45 km s^{-1} channel. We mainly focus on the small beam size ($2''.3 \times 1''.6$) in the following discussion.

2.2. 250 GHz Dust Continuum

We imaged the observed frame 250 GHz continuum emission of the MAMMOTH-1 field with NOEMA in C configuration (ID: W19CX). The observations were carried out on 2019 December 29 and 31, using the PolyFiX correlator with the full available continuum bandwidth of 15.5 GHz in dual polarization. The flux scale was calibrated on MWC349 and the phase was checked with the calibrator 1505+428 close to our target. The total observing time is 8 hr with 5 hr on-source. The primary beam for NOEMA observations at $\nu_{obs} = 250$ GHz ($\nu_{rest} \sim$ 828.2 GHz) are 21″. The FWHM synthesized beam size is $0''.87 \times 0''.65$ and the position angle is 49°. The final continuum 1σ rms sensitivity in the central region of the cleaned image is 0.04 mJy beam^{-1}. Primary beam correction was applied to the final flux measurements described in Section 3.4.

Table 2
Physical Properties of the Protocluster Core MAMMOTH-I

Source	L_{FIR} $10^{11}\ L_\odot$	SFR $M_\odot\ yr^{-1}$	$L'_{CO(1-0)}$ 10^{10} K km s^{-1} pc^2	$L'_{CO(3-2)}$ 10^{9} K km s^{-1} pc^2	$r_{3,1}$	M_{gas} $10^{10}\ M_\odot$
(1)	(2)	(3)	(4)	(5)	(6)	(7)
G1(A)	13.0 ± 2.6	224 ± 45	1.2 ± 0.3	7.1 ± 1.1	0.59 ± 0.17	4.3 ± 0.1
G2(B)-narrow	5.1 ± 1.1	88 ± 19	1.1 ± 0.2	6.7 ± 1.4	0.61 ± 0.17	4.0 ± 0.1
G2(B)-broad			0.7 ± 0.4		0.91 ± 0.51	
G3	<2.1	<36	<0.9	3.0 ± 1.1	>0.33	2.1 ± 0.8
G4	<2.1	<36	<0.9	3.7 ± 0.9	>0.41	2.6 ± 0.6
G5	<2.1	<36	<0.9	2.1 ± 0.6	>0.24	1.5 ± 0.4
G6(C)	3.2 ± 0.9	54 ± 15	1.0 ± 0.4	5.4 ± 1.2	0.54 ± 0.25	3.6 ± 0.1

Note. Col. (1): Source name. Col. (2): FIR luminosity from 8 to 1000 μm, assuming a modified blackbody for optically thin thermal dust emission, with a dust temperature of 42K for *Source B* (as it is a Type II AGN) and 35K for other galaxies. We adopt an emissivity index of $\beta = 1.6$, which is the typical value found in FIR-bright quasars at $z \sim 2$–4 (Beelen et al. 2006). Given upper limits are 3σ. Col. (3): star-formation rate. Here we use SFR $= 4.5 \times 10^{-44} \times L_{FIR}$ (Kennicutt 1998). Col. (4): CO(1 − 0) luminosity of the ELAN MAMMOTH-I from Emonts et al. (2019). Col. (5): CO(3 − 2) luminosity from our NOEMA observations. Col (6): CO(3 − 2) /CO(1 − 0) line ratio. The fitted broad and narrow components of G2 are discussed in Section 4.2, which trace the center galaxy and the extended CGM gas, respectively. Col (7): molecular gas mass, assuming a typical conversion factor for high-z galaxies of $\alpha_{CO} = M_{H2}/L'_{co} = 3.6\ M_\odot$ (K km s^{-1} pc^2)$^{-1}$ (e.g., Daddi et al. 2010; Genzel et al. 2010). Gas masses for G1, G2 and G6 are derived from $L'_{CO(1-0)}$ (Emonts et al. 2019). We assume that the other three galaxies are star-forming-dominated galaxies $r_{3,1} = 0.52$ and derive gas mass from $L'_{CO(3-2)}$.

2.3. Ancillary Data

The rest-frame optical deep image of the MAMMOTH-I field was obtained using the Hubble Space Telescope (HST) Wide Field Camera 3 (WFC3) with the F160W filter (ID: 14760). The observation was carried out in Cycle 24 with an exposure time of ∼2665 s; we use nine HST/WFC3 pointings to cover this central region in nine orbits to measure the detailed rest-frame optical morphology. The data reduction is conducted using Multidrizzle (Koekemoer et al. 2003) and the detailed procedures follow the descriptions in Cai et al. (2016). To optimize the output data quality, we choose a final output pixel scale of 0.″06 instead of the initial pixel scale 0.″13 and final pixfac parameter 0.7 (shrinking pixel area) after different trials of combinations of parameters.

We also observed the Lyα line of MAMMOTH-I with the Keck Cosmic Web Imager (KCWI) on the Keck II telescope of the W. M. Keck Observatory in Hawaii in 2018 May (seeing ∼1.″5). The on-source exposure time is 1 hr. We used the Blue Medium Grating with the Large Slicer (slice width ∼3.″5), resulting in a spectral resolution of 2000 and field of view of $33'' \times 20''$, centered on *Source B*, the quasar optical position given by Cai et al. (2017b). To convert the spectral images and calibration frames (arcs, flats, bias) to a calibrated data cube, we used the IDL-based KCWI data reduction pipeline.[14] Basic CCD reduction is performed on each science frame to obtain a bias-subtracted, cosmic-ray-cleaned and gain-corrected image. The continuum flat images are employed for CCD response corrections and pixel-to-pixel variations. We used a continuum-bar image and an arc image (ThAr) to define the geometric transformations and wavelength calibration, generating a rectified object data cube (see the pipeline documents[15]). Twilight flats were used for slice-to-slice flux correction, and the data were corrected for atmospheric refraction. Each object and sky frame was flux calibrated with the standard star BD28d4211. For each exposure we found the QSO centroid to measure the offsets between exposures and then performed a weighted mean with inverse-square variance weighting to construct the final data cube.

[14] Available at https://github.com/kcwidev/kderp/releases/tag/v0.6.0.
[15] https://github.com/kcwidev/kderp/blob/master/AAAREADME

The CO(1 − 0) line data of this field was observed using the Very Large Array (VLA) in the most compact D-configuration and published in Emonts et al. (2019), which is included in the analysis of this paper. The exposure time is 14 hr on-source, with an rms noise level of 0.057 mJy beam^{-1} channel^{-1}, for a channel width of 30 km s^{-1}. The field of view (primary beam) for VLA observations at $\nu_{obs} \sim 34.81$ GHz ($\nu_{rest} = 115.27$ GHz) is 1.′3. The synthesized beam is $2.''6 \times 2.''3$. We use these near-infrared and radio data to compare with our CO(3 − 2) observations in order to study the molecular gas distribution and kinematics and thus provide a link between the ELAN and the stellar build-up of this system.

3. Results

Within the central 16″ region of ELAN MAMMOTH-1, we detect strong CO(3 − 2) emission in six proximate galaxies. The velocity-integrated CO intensity maps are shown in Figure 1. These sources are all $>3\sigma$ detections in CO(3 − 2) and have HST optical counterparts. Three of them are also detected in CO(1 − 0) with the VLA (Emonts et al. 2019). Figure 2 shows the intensity map of the CO(3 − 2) emission and the spectra extracted from the peak of the CO(3 − 2) detections. The intensity map is the integrated intensity over the line-emitting region. The selected velocity ranges for each source are shown in the yellow channels in the right side of Figure 2. In the right panels of Figure 2, we did not detect any continuum; we fit the spectra with a Gaussian profile, then calculated the line center, full width half maximum (FWHM), and line flux. The derived results are summarized in Table 1. The spectroscopic redshifts of the sources ($z_{spec} = 2.3037 - 2.3137$, in a range from −770 to +120 km s^{-1}) are all consistent with being physically related to the same structure at $z = 2.3$.

3.1. CO(3 − 2) Line Detections of Individual Sources

At the center of the ELAN MAMMOTH-1, the CO(3 − 2) line flux of *Source B* (G2) is 0.237 ± 0.051 Jy km s^{-1} (Figure 2). We fit the FWHM $_{CO(3-2)}$ to be 370 ± 90 km s^{-1}, which is a typical CO line width found in samples of SFGs and quasars (e.g., Carilli & Walter 2013; Ueda et al. 2014). However, the line width of the CO(1 − 0) detected in Emonts et al. (2019) is much

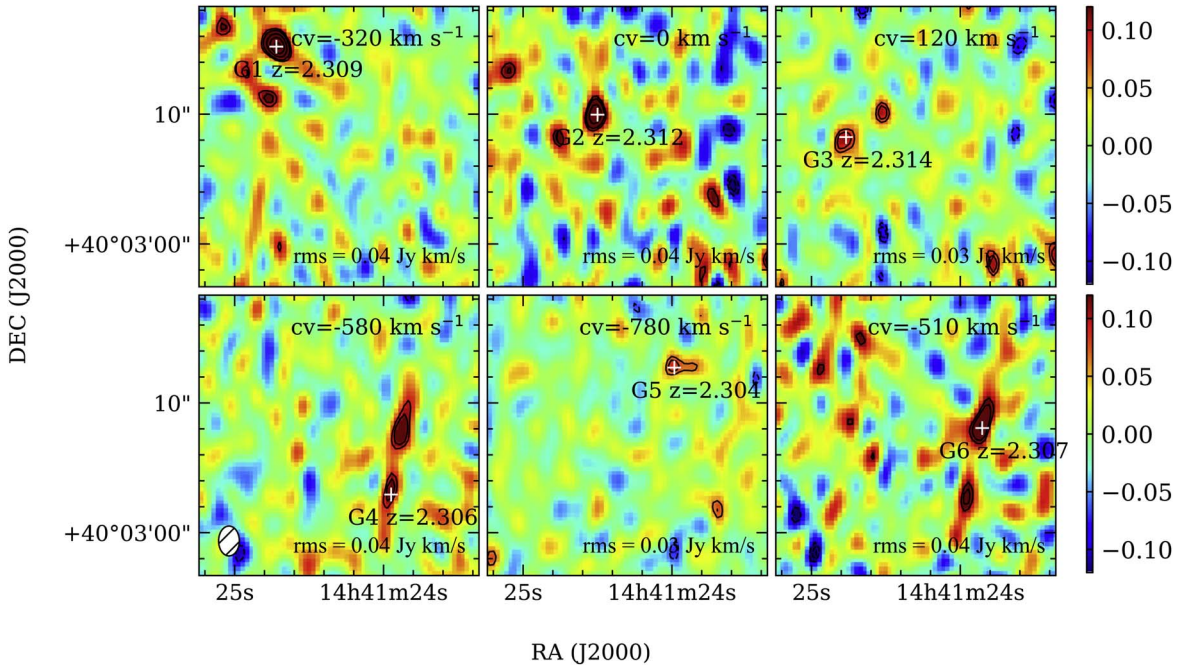

Figure 1. The velocity-integrated CO(3 − 2) intensity map (∼20″ × 20″) of 3σ detected sources around the ELAN MAMMOTH-I in NOEMA observations. The contour levels are [−3, −2.5, +2.5, +3, +4, +5...] × σ, with σ = [0.03–0.04] Jy beam^{-1} km s^{-1}. The map has been made the primary beam correction. The integrated velocity ranges are shown in the yellow channels on the right side of Figure 2. The center velocity ("cv") is the offset velocity of the CO(3 − 2) peak emission respect to G2 (source B). The rms is also marked on the individual map.

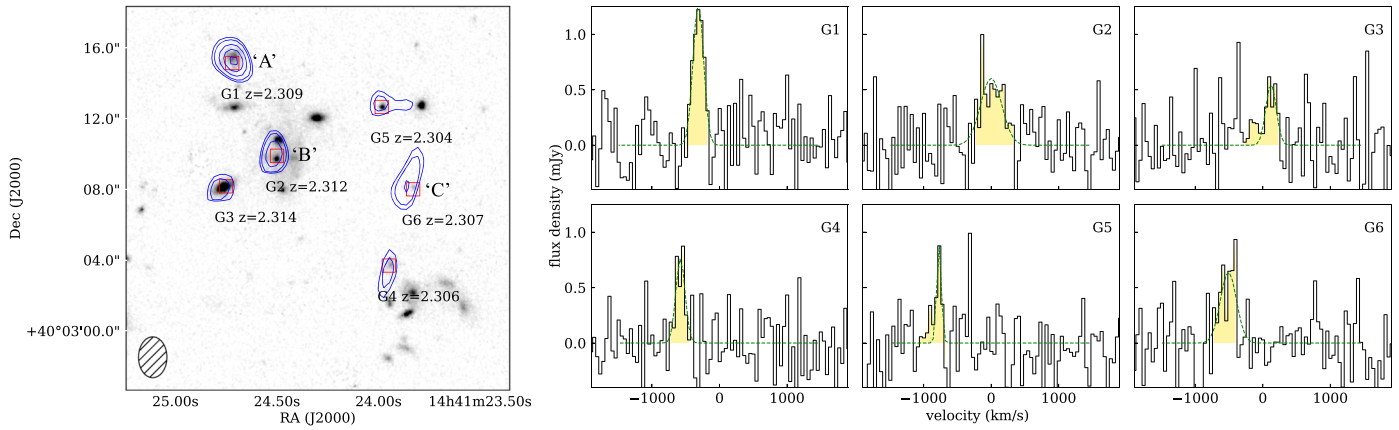

Figure 2. CO(3 − 2) emission of the galaxies detected around the ELAN MAMMOTH-I (approximately centered on G2) using NOEMA. (a) The left panels show the members of the galaxy group (∼20″ × 20″) confirmed by CO(3 − 2) emission, overlaid on the HST F160W image. The CO(3 − 2) intensity map has been made the primary beam correction. The contour levels are [+2.5, +3, +4, +5...] × σ, with σ = [0.03–0.04] Jy beam^{-1} km s^{-1}. The NOEMA beam (2.″3 × 1.″6) is denoted by the ellipse. (b) The right panels show the one-dimensional spectra of these CO emission-line detections, extracted from the detection peak (marked as the square in the left panel). The root-mean-square (rms) noise level is 0.3 mJy beam^{-1} per 45 km s^{-1} channel. *Source B* (G2) is the center of the Lyα; the zero velocity of all the spectra corresponds to Source "B" at z = 2.3123. The area filled with colors indicates the regions where emission is detected. The green dashed lines are the Gaussian fit.

narrower, only 85 km s^{-1}. We re-analyze the previous CO(1 − 0) data, fitting it with a double Gaussian profile with no constraint applied. After subtracting the narrow Gaussian component, the line width of the new broad CO(1 − 0) component is similar to that of CO(3 − 2) . More details are presented in Section 4.2. The redshift derived from CO(3 − 2) line is $z_{\rm CO} = 2.3123 \pm 0.0006$, while the redshift derived from Lyα is $z_{Ly\alpha} = 2.329 \pm 0.013$ (Cai et al. 2017b). This shift may be due to resonant scattering of Lyα. The 2D Gaussian fit for the velocity-integrated image suggests line emission from an unresolved source.

Figure 2 also reveals two bright sources in CO(3 − 2) in the nearby region of *Source B*, labeled as *Sources A* and *C*. They were detected in CO(1 − 0) line emission down to a sensitivity level of 0.057 mJy beam^{-1} channel^{-1} for a channel width of 30 km s^{-1} (Emonts et al. 2019). Adopting the naming convention from Emonts et al. (2019), *Source A* (G1) is the brightest detection in both CO(3 − 2) and CO(1 − 0) lines in these systems. However, it is not located inside the ELAN MAMMOTH-I (6″ away from *Source B*) and has its own Lyα emission (Q. Li 2021, in preparation). It is also unresolved. The line flux $I_{\rm CO(3-2)}$ is 0.298 ± 0.044 Jy km s^{-1}.

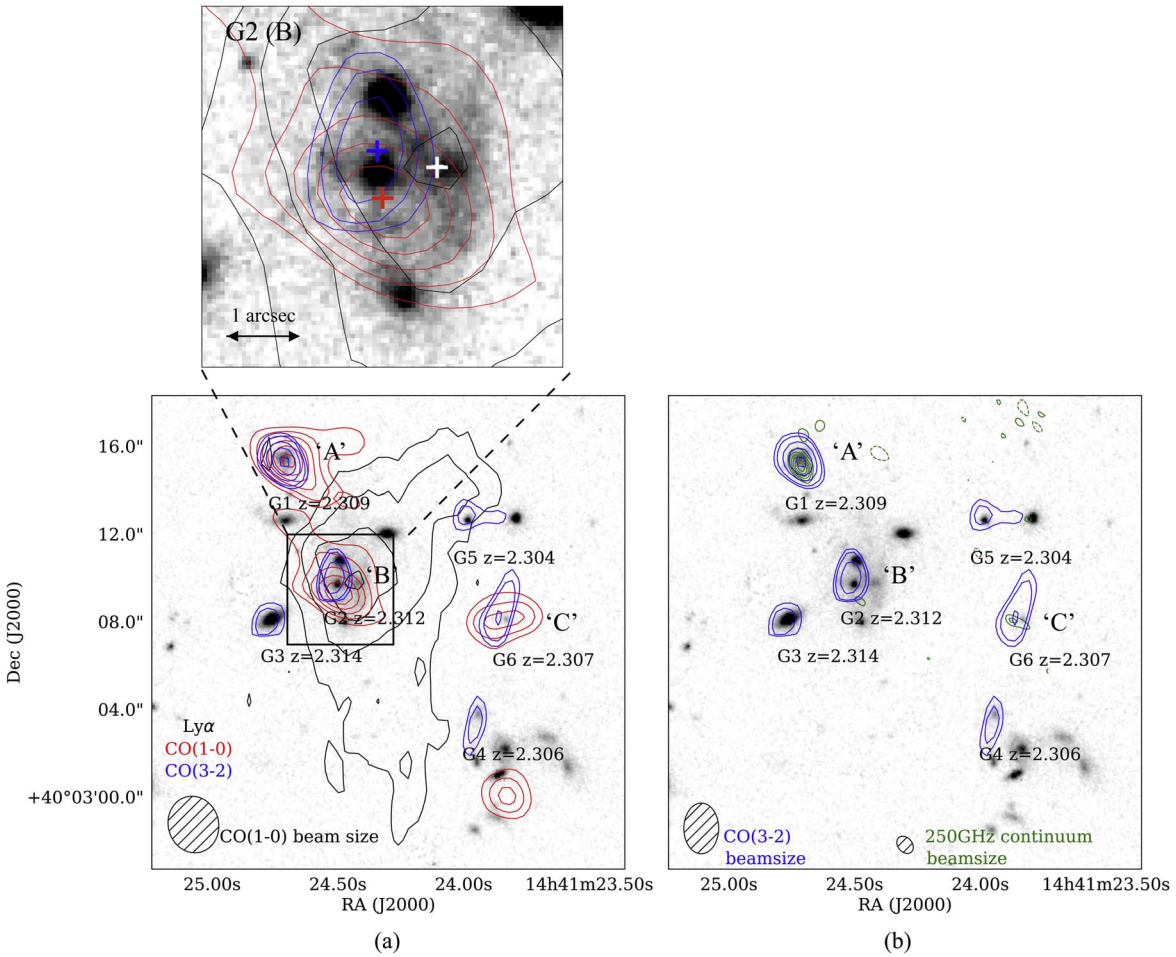

Figure 3. (a) CO(3 − 2) emission from NOEMA (blue contours), CO(1 − 0) from VLA (red contours) and Lyα from KCWI (black contours, Q. Li et al. 2021, in preparation) overlaid onto the HST/WFC3 FW160W image (Z. Cai et al. 2021, in preparation). Six sources of this galaxy group (or a so-called protocluster core) are detected with NOEMA; three of them are also detected in CO(1 − 0) with the VLA. The Lyα contours levels are [+2.5, +7.5, +22.5, +45.0] × 0.04 mJy beam^{-1}. The CO(1 − 0) and CO(3 − 2) contours levels are [+2.5, +3.5,...] × σ. The synthesized beam of CO(1 − 0) is $2\farcs6 \times 2\farcs3$, the synthesized beam of CO(3 − 2) is $2\farcs3 \times 1\farcs6$. The synthesized beam at 250 GHz is $0\farcs87 \times 0\farcs75$. The upper panel shows a zoom around *Source B*. The white, blue, and red crosses indicate the peak of Lyα, CO(3 − 2), and CO(1 − 0). (b) 250 GHz dust continuum and CO(3 − 2) emission from NOEMA (green and blue contours) overlaid onto the HST/WFPC3 image. Three galaxies in the galaxy group have above 3σ continuum detections. The 250 GHz continuum contours levels are [−4, −3, +3, +4, +5, +6, ...] × σ. The continuum sensitivity is 0.04 mJy beam^{-1}.

Its FWHM $_{CO(3-2)}$ of $\sim$180km s^{-1} is similar to that of CO(1 − 0) ($\sim$170km s^{-1}). *Source C* (G6) is a faint detection roughly 9″ west of *Source B* with a line flux of 0.245 ± 0.056 Jy km s^{-1}. The line width is FWHM $_{CO(3-2)} = 280 \pm 70$ km s^{-1}, similar to the CO(1 − 0) of $\sim$230 km s^{-1}. The velocity offset relative to *Source B* is $\sim$510 km s^{-1}.

The other three sources (G3, G4, G5) are all >3σ detections in CO(3 − 2) and have HST optical counterparts. However, they are not detected in CO(1 − 0) . By applying the line ratio of $r_{3,1} = 0.52$ for SFGs (Kirkpatrick et al. 2019), the 1σ rms of the VLA CO luminosity measurement of $L'_{CO(1-0)} \sim 0.3 \times 10^{10}$ K km s^{-1} pc^2 would correspond to $L'_{CO(3-2)} \sim 1.6 \times 10^9$ K km s^{-1} pc^2 for CO(3 − 2). The sensitivity of the VLA observations is insufficient to detect the CO(1 − 0) line from these three objects.

3.2. The Distribution of the CO(3 − 2) Emission

Now we compare CO, Lyα, and optical counterparts of this system. In Figure 3 we show the map of the CO(3 − 2) line emission from NOEMA (blue contours), CO(1 − 0) from VLA (red contours), and the Lyα from KCWI (black contours, Q. Li et al. 2021, in preparation) overlaid on the HST/WFC3 FW160W image (Z. Cai et al. 2021, in preparation). The HST image shows four optical counterparts around *Source B*, see Figure 3(a). The CO(3 − 2) and CO(1 − 0) peaks of *Source B* (G2) are almost consistent with the central HST optical source. The peak of Lyα is located at another optical counterpart. The CO peak and Lyα peak have an offset of $\sim$1.5″ ($\sim$13kpc). Taking into account the accuracy of the radio interferometric positions[16] from the VLA and NOEMA, and the seeing of the Lyα observations of $\sim 1\farcs0$, the offset could be real.

Source A (G1) has an optical counterpart in the HST image. It was also detected Lyα emission, 7″ away from the Lyα peak of the ELAN MAMMOTH-I. The CO(3 − 2) peak of *Source A* (G1) coincides with CO(1 − 0) . Emonts et al. (2019) reported that the CO(1 − 0) emission of *Source A* and *Source B* have extended features of $\sim$25 kpc and 30 kpc, respectively. However, our CO(3 − 2) observations suggest that they are

[16] The radio interferometric position measurement uncertainty of *Source B* ($\Delta\theta \sim 0.5\frac{\theta_{\rm beam}}{\rm SNR}$, Reid et al. 1988) using NOEMA and VLA are $\sim 0\farcs2$ and $0\farcs2$, respectively

unresolved, which implies that CO(3 − 2) is compact and emitted from the star-forming region within the galaxy.

Source C (G6) does not have any Lyα counterpart but shows an HST optical detection. *Source C* also has CO(1 − 0) emission in VLA observations (Emonts et al. 2019). The CO(1 − 0) and CO(3 − 2) lines also show that it is a point source. Its CO(3 − 2) line flux is weaker than for A and B.

The maximum recoverable scale is ∼41″ for our CO(3 − 2) observations, corresponding to the physical scale of ∼340 kpc at $z \sim 2.3$. Here we tapered the beam to recover the additional emission in CGM with a beam size of 3.″2 × 3.″2, corresponding to a physical scale of ∼27 kpc. We assumed the same average $r_{3,1} = 0.6$ and the same CO line width in the CGM; the sensitivity of CO(1 − 0) in VLA data is 0.057 mJy beam^{-1} per 30 km s^{-1} channel and the derived sensitivity of CO(3 − 2) is 0.5 mJy beam^{-1} per 45 km s^{-1} channel. Our NOEMA data sensitive is 0.4 mJy beam^{-1} per 45 km s^{-1} channel, enough to detected the CO(1 − 0) extended features in CO(3 − 2), but at this sensitivity in our NOEMA data, we did not detect diffuse CO(3 − 2) emission. This indicates that there is no diffuse CO(3 − 2) line emission across the nebula. It is different from the diffuse CO(1 − 0) emission which appears extended across a region of ∼30 kpc.

3.3. Line Ratios

To constrain the nature of the sources of this system, here we calculate the CO(3 − 2) line luminosity of each source as $L'_{\rm CO} = 3.25 \times 10^7 \times I_{\rm CO} D_L^2 (1+z)^{-3} \nu_{\rm obs}^{-2}$ K km s^{-1} pc^2 (Solomon et al. 1992) where $I_{\rm CO}$ is the integrated line flux in Jy km s^{-1}, D_L is the luminosity distance in Mpc and $\nu_{\rm obs}$ is the observing frame CO(3 − 2) line frequency. The derived line luminosities are in the range of $(2.1-7.1) \times 10^9$ K km s^{-1} pc^2. The CO(3 − 2)/CO(1 − 0) luminosity ratios ($r_{3,1}$) of *Sources A*, *B*, and *C* are 0.59 ± 0.17, 0.61 ± 0.17, and 0.54 ± 0.25, respectively. The median line ratios $r_{3,1}$ for AGN- and star-formation-dominated galaxies are 0.92 ± 0.44 and 0.52 ± 0.17 (Kirkpatrick et al. 2019). Carilli & Walter (2013) suggested the average line ratio $r_{3,1}$ of quasars is 0.97. *Source B* is lower than this value and lies toward the low end of the expected AGN-dominated range.

Low $r_{3,1}$ in ELANe have also been reported previously, e.g., Genzel et al. (2003) observed SMM J02399, a BAL quasar in a >140 pkpc ELAN at $z \sim 2.8$ (Ivison et al. 1998; Li et al. 2019). Its $r_{3,1}$ is 0.48 ± 0.13. By contrast, the central radio galaxy MRC 1138–262 in the ELAN Spiderweb Galaxy (Lyα extended ∼200 kpc, Miley et al. 2006) shows a very high global $r_{4,1}(L'_{\rm CO(4-3)}/L'_{\rm CO(1-0)})$ of 1.00 ± 0.28 (Emonts et al. 2018). Its CGM has $r_{4,1} = 0.45 \pm 0.17$, similar to SFGs.

Regardless of the presence of AGNs, the ratios $r_{3,1}$ in different galaxies vary greatly from 0.4 to 0.9. At high z, the literature, such as Harris et al. (2010; $z = 2.5 - 2.9$ SMGs) and Aravena et al. (2010; $z \sim 1.5$ normal SFGs), reports $r_{3,1} \sim 0.6$. Sharon et al. (2016) report that there is no statistically significant difference in the mean line ratio ($r_{3,1} = 0.90 \pm 0.40$ for both populations combined) in $z \sim 2$ galaxies including both AGNs and SMGs. Furthermore, Riechers et al. (2020) report $r_{3,1} = 0.84 \pm 0.26$ in $z = 2 - 3$ main-sequence galaxies from the ASPECS surveys. The higher-J CO transition observations, at least $J_{\rm up} \geq 4$, can further reveal the excited gas and especially excitation from AGNs.

3.4. 250 GHz Continuum and FIR Luminosity

Previous continuum observation of MAMMOTH-1 using SCUBA-2 at the observed frame 350 GHz revealed bright dust-continuum emission with a flux of $S_{350\rm GHz} = 4.6 \pm 0.9$ mJy (Arrigoni Battaia et al. 2018b). However, the SCUBA-2 beam size of 15″ is too large to constrain the continuum emission from individual galaxies. All the CO-detected objects in this area could contribute to the SCUBA-2 flux. Three continuum sources are detected at >4σ in this field from our NOEMA 250 GHz (1.2mm at observed frame) map at $0.''87 \times 0.''65$ resolution. They are counterparts of the CO detections described above (Sources A, B, and C). We used 2D Gaussian fitting to measure the continuum and detect a continuum flux of 0.74 ± 0.15 mJy from Source A. The continuum emission is marginally resolved along the major axis with a deconvolved source size of $(1.25 \pm 0.32)'' \times (0.57 \pm 0.26)''$. This is the brightest continuum detection in the MAMMOTH-1 field. We detect a 4σ continuum source at the position of Source B. The continuum emission is unresolved and we adopt the peak surface brightness as the total continuum flux which is 0.14 ± 0.03 mJy. We also detect continuum emission from Source C with a flux of 0.18 ± 0.05 mJy. The source is unresolved as well. The continuum detections are summarized in Table 1.

The NOEMA continuum map at 250 GHz allows us to determine the FIR luminosity and the star-formation rate. We assume a modified blackbody for optically thin thermal dust emission, with the dust temperature of 42K for *Source B* (AGN), and 35 K for other galaxies. We adopt an emissivity index of $\beta = 1.6$ (Beelen et al. 2006). For the non-detections, we adopt a 3σ upper limit. We estimate FIR luminosity by integrating the modified blackbody function in 8–1000 μm anchored by 250 GHz flux measurement. The derived FIR luminosity of *Source A*, *Source B*, and *Source C* is (13.0 ± 2.6), (5.1 ± 1.1), and $(3.2 \pm 0.9) \times 10^{11} L_\odot$. In Figure 4, we compared these galaxies around ELAN MAMMOTH-I with other quasar samples, intermediate-z ULIRGs, normal SFGs and SMGs (Bothwell et al. 2013; Carilli & Walter 2013; Riechers 2013; Magdis et al. 2014; Cañameras et al. 2015; Daddi et al. 2015; Harrington et al. 2016; Strandet et al. 2017; Yang et al. 2017; Arabsalmani et al. 2018; Dannerbauer et al. 2019). The FIR luminosities of the galaxies in MAMMOTH-I are slightly lower than that of quasars but still consistent with normal SFGs; see Figure 4, right panel). The CO–FIR luminosity ratios for the MAMMOTH-I members are at the lower end but still follow the trend of the relation between $L_{\rm IR}$ and $L'_{\rm CO(3-2)}$. This indicates that these galaxy members are all following the star-formation law, in which the star-formation rate traced by the IR luminosity has a tight relation with the mass of fuel traced by CO(3 − 2).

The derived total FIR luminosity of the whole nebula from the 250 GHz observations is $<2.7 \times 10^{12} L_\odot$. Arrigoni Battaia et al. (2018b) reported a bright detection at observed frame 350 GHz (850 μm), with a flux of $S_{350\ \rm GHz} = 4.6 \pm 0.9$ mJy (with a beam size of 15″) and a 3σ upper limit of about 16 mJy at observed frame 667 GHz (450 μm). The group of six galaxies are all covered by the 350GHz SCUBA-2 beam (∼15″). The total flux at the observed frame 250 GHz is <1.42 mJy. Assuming the modified blackbody for *Source B* (AGN; $T_{\rm dust} = 42$ K, $\beta = 1.6$) and other galaxies ($T_{\rm dust} = 35$K, $\beta = 1.6$), the derived total 350GHz flux should be <3.7 mJy. The results are slightly lower than the SCUBA-2 detections.

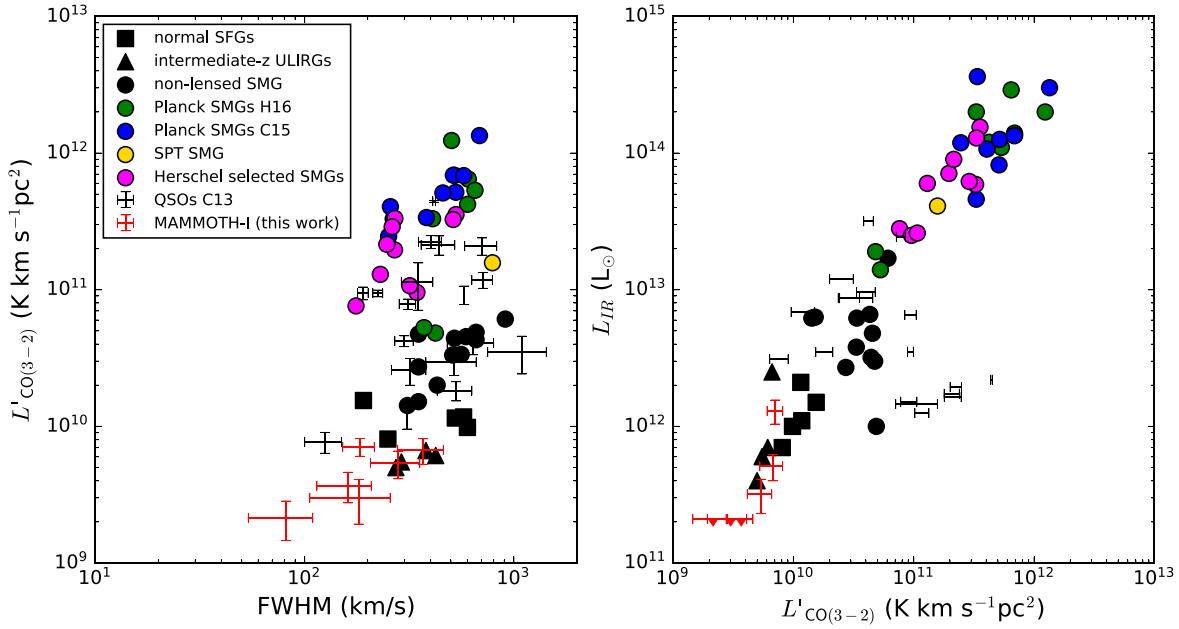

Figure 4. Left: the relation between FWHM and $L'_{CO(3-2)}$ of the high-redshift galaxies and quasars. The galaxies in MAMMOTH-I are shown in red. The comparable quasar sample is from Carilli & Walter (2013). The comparable galaxies from the literature are as follows: intermediate-z ULIRGs (black filled triangles: Magdis et al. 2014), normal SFGs (black filled squares: Daddi et al. 2015; Arabsalmani et al. 2018), nonlensed SMGs (black filled circles from Bothwell et al. 2013), Herschel-selected lensed SMGs (magenta filled circles: Riechers 2013; Yang et al. 2017), SPT-selected lensed SMG (gold filled circle; Strandet et al. 2017), Planck-selected SMGs from Harrington et al. (2016; green filled circles) and Cañameras et al. (2015; blue filled circles). Right: the relation between L_{IR} and $L'_{CO(3-2)}$.

This may be due to the standard matched filter applied in the SCUBA-2 data reduction in order to increase the point source detectability (Arrigoni Battaia et al. 2018b).

Assuming a star-formation-powered emission, we estimate the star-formation rate as $SFR/M_\odot\ yr^{-1} = 4.5 \times 10^{-44} \times L_{FIR}/erg\ s^{-1}$ (Kennicutt 1998); see Table 2. The three sources detected at 250 GHz are violent starbursts with a star-formation rate ranging between 54–224 $M_\odot\ yr^{-1}$.

4. Discussion

4.1. Halo Mass of Protocluster Core

MAMMOTH-I resides in the density peak of the large-scale structure BOSS1441, which is one of the most overdense fields discovered to date with an LAE density 12 times higher than that of a random field density on a 15 cMpc scale. We discovered a remarkable galaxy concentration at a redshift of $z \sim 2.3$, containing six gas-rich galaxies spectroscopically confirmed through the CO(3 − 2) transition in the central ∼100 kpc region. The high density of massive galaxies and velocity dispersion of this overdensity suggest that it could be embedded in a collapsed, cluster/group-sized halo. In this section, we further explore the total halo mass of this galaxy group.

Galaxy cluster velocity dispersion provides a reliable estimate of the cluster mass (Evrard et al. 2008; Munari et al. 2013; Saro et al. 2013; Wang et al. 2016). The cluster redshift is $z = 2.308$, determined by the weighted average of the CO(3 − 2) redshifts of these six galaxies. The galaxy proper velocities v_i are then derived from their redshifts z_i by $v_i = c(z_i - z)/(1 + z)$ (Danese et al. 1980). The line-of-sight velocity dispersion σ_v is the square root of the weighted sample variance of proper velocities (Beers et al. 1990; Ruel et al. 2014) which is estimated to be $\sigma_v = 320\ km\ s^{-1}$. We assume that only the inner portion of this protocluster is virialized. Using the relation between velocity dispersion and total mass suggested in Evrard et al. (2008), $\sigma_{DM}(M, z) = \sigma_{DM,15}(h(z)M_{200c}/10^{15}M_\odot)^\alpha$, we derive a total halo mass of ELAN MAMMOTH-I of $M_{200c} \sim 10^{13.1} M_\odot$ (by using the canonical value of $\sigma_{DM,15} \sim 1083 km\ s^{-1}$ and the logarithmic slope $\alpha \sim 0.33617$). It is an upper limit if the system has not yet virialized. The previous studies of AGNs, SMGs, and bright LABs show that they are expected to live in halos of $10^{12-14}\ M_\odot$ (e.g., Yang et al. 2010; White et al. 2012; Wang et al. 2016; Wilkinson et al. 2017). The total halo mass of the ELAN MAMMOTH-I is in a good agreement with that of AGNs and SMGs.

Previous work on protocluster cores based on sensitive observations of CO and ionized carbon (Miller et al. 2018; Oteo et al. 2018; Gómez-Guijarro et al. 2019) reported total molecular gas masses of $\sim 10^{11} M_\odot$ and a total halo mass as high as $\sim 10^{13} M_\odot$. We use $L'_{CO(1-0)}$ from Emonts et al. (2019) to derive the cold molecular gas mass M_{H2} for *Source A*, *Source B*, and *Source C*. The gas masses are in the range of $(3.6–4.3) \times 10^{10} M_\odot$. Here we assume a typical conversion factor for high-z galaxies of $\alpha_{CO} = M_{H2}/L'_{co} = 3.6\ M_\odot\ (K\ km\ s^{-1}\ pc^2)^{-1}$ (e.g., Daddi et al. 2010; Genzel et al. 2010). For the other three galaxies without detections of CO(1 − 0) we assume a gas excitation similar to typical SFGs with $r_{3,1} = 0.52$. Their gas masses derived from $L'_{CO(3-2)}$ in our NOEMA observations are in the range of $(1.5–2.6) \times 10^{10} M_\odot$, which is listed in Table 2. The total molecular gas mass in the MAMMOTH-1 protocluster is $1.8 \pm 0.1 \times 10^{11} M_\odot$. In summary, the gas, dust, and stellar properties of MAMMOTH-I are all comparable to these protocluster cores mentioned before, indicating that MAMMOTH-I should be the progenitor of a galaxy cluster.

Finally, we note that due to the influence of large-scale structure in and around clusters (White et al. 2010), there are uncertainties in the estimation of the mass for an individual cluster based on velocity dispersion. We are also aware that the

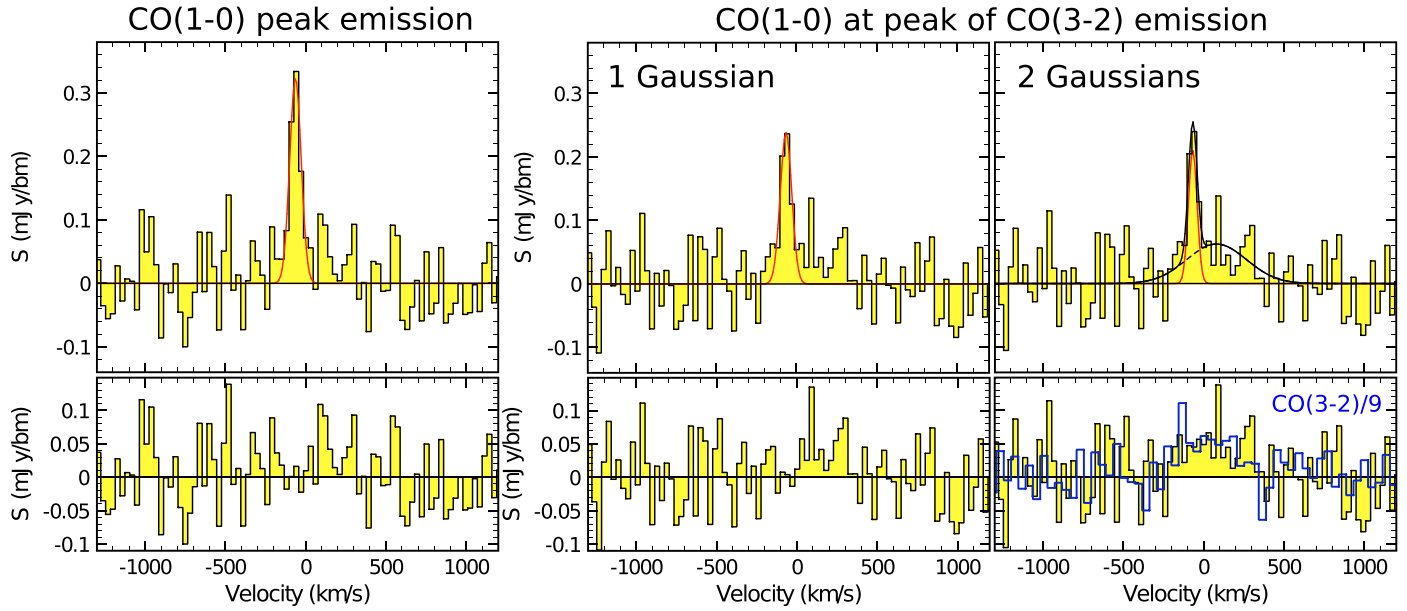

Figure 5. The intensity spectra of CO(1 − 0) in region B, taken at the location of the peak of the CO(1 − 0) (left) and at the location of the peak of the CO(3 − 2) emission (right). These locations are marked with the red and blue "+" sign in Figure 3, respectively. The spectra are not mutually independent, because both locations fall within the same synthesized beam in the CO(1 − 0) data, meaning that features with sufficient signal-to-noise appear in both spectra. The spectrum on the left is fitted with a single Gaussian function from Emonts et al. (2019). On the right, the top panels show the same spectrum, with the first panel showing a single Gaussian with width constrained to that of the CO(1 − 0) peak emission (FWHM = 85 km s^{-1}), and the second panel showing a double Gaussian fit with no constraints applied. The bottom panels show the residuals after subtracting the narrow (red) Gaussian component from each spectrum. In the bottom right-hand panel, a weak, broad CO(1 − 0) component is present at the peak of the CO(3 − 2) emission. Overlaid in blue is the CO(3 − 2) spectrum, scaled down by a factor of nine for easy comparison.

sample used to estimate the velocity dispersion only includes SFGs. The quiescent galaxies would also change the estimate of the velocity dispersion (Wang et al. 2016). As we cannot rule out completely the existence of quiescent galaxies of this galaxy cluster, we are planning to confirm more member galaxies spectroscopically to further improve the accuracy of the velocity dispersion estimation.

4.2. The CGM within MAMMOTH-1

Extended CO(1 − 0) emission has been found on the scale of tens of kpc around high-z massive galaxies or in protoclusters (e.g., Emonts et al. 2014, 2016; Dannerbauer et al. 2017). For ELAN MAMMOTH-I, Emonts et al. (2019) also reported that half of the cold molecular gas traced via the CO(1 − 0) transitions stretches on ∼30 kpc into the CGM, appearing to be a wide tail of gas in *Source A*(*G*1) and an extended reservoir of cold gas in *Source B*(*G*2). Extended high-*J* CO emission in the CGM has also been reported in some metal-line nebulae. Ginolfi et al. (2017) detected a large structure of molecular gas reservoir traced by CO(4 − 3) in an [O III] nebula, extending over 40 kpc. Strikingly, with our NOEMA observations, we did not find any evidence of extended CO(3 − 2) emission.

This could be due to the fact that the critical density of CO (J, $J-1$) scales roughly with $n_{\rm crit} \propto J^3$. The ground-transition CO(1 − 0) has an effective critical density of only several 100 cm^{-3} and the $J = 1$ level of CO is substantially populated down to $T \sim 10$ K. However, these values increase by an order of magnitude or more for the high-*J* transitions, like CO(3 − 2) and higher. Compared to CO(1 − 0), the CO(3 − 2) is more likely a tracer of the star-forming region or compact gas around an AGN. As in such regions, the gas is warmer and denser compared to that in the CGM. CO molecules tend to populate at high-J levels, and the optical depth also increases.

In the CGM around *Sources A* and *B*, the molecular gas is not excited to give strong CO(3 − 2) emission. The ELANe Slug ($z = 2.282$) and Jackpot ($z = 2.041$) also do not show any extended CO(3 − 2) emission (Decarli et al. 2021), whereas, for the ELAN around the Spiderweb Galaxy, CO(4 − 3) (and [C I]) are detected across ∼50 kpc, comprising ∼30% of the total flux. The Spiderweb Galaxy has a massive, cold molecular gas reservoir in the CGM that is roughly twice as luminous as that seen in CO(1 − 0) in MAMMOTH-I (Emonts et al. 2016, 2019). In addition, the Spiderweb Galaxy emits jets of relativistic particles visible in radio observations and has a metal-enriched outflow (Pentericci et al. 1997; Nesvadba et al. 2006). By contrast, MAMMOTH-1 does not have a radio jet and does not show any clear features of outflow in [C IV] and [He II] observations (S. Zhang et al. 2021, in preparation). These could explain the reason why CO(3 − 2) around ELAN MAMMOTH-I is only associated with galaxies but not with the CGM.

In Figure 5 we revisit the CO(1 − 0) analysis of *Source B* from Emonts et al. (2019) and compare its CO(3 − 2) and CO(1 − 0) transitions. The CO(3 − 2) line shows a broad line profile with FWHM of ∼350 km s^{-1}. It is comparable to the typical line width of SMGs (e.g., Bothwell et al. 2013; Carilli & Walter 2013; Goto & Toft 2015) which implies that CO(3 − 2) traces the molecular gas from the star-forming regions within the galaxy. By comparison, while the CO(1 − 0) signal in *Source B* is dominated by a narrow CO(1 − 0) line (FWHM of 85 km s^{-1}) outside the central galaxies, at the location of the peak of the CO(3 − 2) emission there appears to be an additional weak, broad component. This broad CO(1 − 0) component is detected only at the 3.2σ level when minimizing the contribution of the narrow component (rightmost panel of Figure 5). However, its properties are remarkably similar to the CO(3 − 2) spectrum in

Source B (G2) with FWHM $= 440 \pm 160$ km s^{-1}, $z = 2.3132 \pm 0.0009$, $I_{CO(1-0)} = 0.029 \pm 0.015$ Jy km s^{-1}, and $r_{3,1} = 0.9 \pm 0.5$. The line ratio value is closer to AGN-dominated molecular gas emission. Therefore, the VLA data are consistent with the presence of two CO(1 − 0) features in *Source B* (G2), namely a CGM component of dynamically cold gas with very low velocity dispersion and excitation conditions (previously described in Emonts et al. 2019) as well as a weak counterpart to the CO(3 − 2) emission of molecular gas associated with the central galaxies. However, for the latter, Figure 5 shows that ambiguities in line-fitting remain and hence deeper CO(1 − 0) observations are needed before drawing any firm conclusions.

5. Summary

In this paper, we present IRAM NOEMA observations of the CO(3 − 2) line and dust continuum at 250 GHz of the ELAN MAMMOTH-1. We discovered a remarkable galaxy concentration, containing 6 massive galaxies in the central ∼100 kpc region, forming a so-called protocluster core. The total halo mass derived from the velocity dispersion is $M_{200c} \sim 10^{13.1} M_{\odot}$. For this ELAN, we did not detect not any extended widespread CO(3 − 2) emission on CGM scales down to our sensitivity of 0.4 mJy beam^{-1} per 45 km s^{-1} channel. Our finding suggests that the CO(3 − 2) emission traces the warmer and denser molecular gas, heated through star formation. Future spectroscopic follow-up observations will confirm more member galaxies in order to better constrain the nature of the ELAN MAMMOTH-1 and its environment which should evolve most likely into a galaxy cluster.

This work was supported by the National Key R&D Program of China (2016YFA0400703) and the National Science Foundation of China (NSFC grants 11721303, 11991052, and 11533001). The National Radio Astronomy Observatory is a facility of the National Science Foundation operated under cooperative agreement by Associated Universities, Inc. This work is based on observations carried out under project numbers S18CW and W19CX with the IRAM NOEMA Interferometer. IRAM is supported by INSU/CNRS (France), MPG (Germany), and IGN (Spain). This work made use of GILDAS,[17] a collection of state-of-the-art software oriented toward (sub-)millimeter radio-astronomical applications (either single-dish or interferometer). R.W. acknowledges support from the Thousand Youth Talents Program of China and the National Science Foundation of China (NSFC) grants No. 11473004 and 11721303. H.D. acknowledges financial support from the Spanish Ministry of Science, Innovation, and Universities (MICIU) under the 2014 Ramón y Cajal program RYC-2014-15686 and under the AYA2017-84061-P, co-financed by FEDER (European Regional, Development Funds), and in addition, from the Agencia Estatal de Investigación del Ministerio de Ciencia e Innovación (AEI-MCINN) under grant (La evolución de los cúmulos de galaxias desde el amanecer hasta el mediodía cósmico) with reference (PID2019-105776GB-I00/DOI:10.13039/501100011033).

ORCID iDs

Qiong Li https://orcid.org/0000-0002-3119-9003
Ran Wang https://orcid.org/0000-0003-4956-5742
Helmut Dannerbauer https://orcid.org/0000-0001-7147-3575
Zheng Cai https://orcid.org/0000-0001-8467-6478
Bjorn Emonts https://orcid.org/0000-0003-2983-815X
Jason Xavier Prochaska https://orcid.org/0000-0002-7738-6875
Fabrizio Arrigoni Battaia https://orcid.org/0000-0002-4770-6137
Roberto Neri https://orcid.org/0000-0002-7176-4046
Chengpeng Zhang https://orcid.org/0000-0001-6469-1582
Xiaohui Fan https://orcid.org/0000-0003-3310-0131
Shuowen Jin https://orcid.org/0000-0002-8412-7951
Ilsang Yoon https://orcid.org/0000-0001-9163-0064
Shane Bechtel https://orcid.org/0000-0003-2851-2924

[17] GILDAS: http://www.iram.fr/IRAMFR/GILDAS.

References

Ao, Y., Zheng, Z., Henkel, C., et al. 2020, NatAs, 4, 670
Arabsalmani, M., Møller, P., Perley, D. A., et al. 2018, MNRAS, 473, 3312
Aravena, M., Carilli, C., Daddi, E., et al. 2010, ApJ, 718, 177
Arrigoni Battaia, F., Chen, C.-C., Fumagalli, M., et al. 2018b, A&A, 620, A202
Arrigoni Battaia, F., Prochaska, J. X., Hennawi, J. F., et al. 2018a, MNRAS, 473, 3907
Beelen, A., Cox, P., Benford, D. J., et al. 2006, ApJ, 642, 694
Beers, T. C., Flynn, K., & Gebhardt, K. 1990, AJ, 100, 32
Bothwell, M. S., Smail, I., Chapman, S. C., et al. 2013, MNRAS, 429, 3047
Cai, Z., Cantalupo, S., Prochaska, J. X., et al. 2019, ApJS, 245, 23
Cai, Z., Fan, X., Bian, F., et al. 2017b, ApJ, 839, 131
Cai, Z., Fan, X., Peirani, S., et al. 2016, ApJ, 833, 135
Cai, Z., Fan, X., Yang, Y., et al. 2017a, ApJ, 837, 71
Cai, Z., Hamden, E., Matuszewski, M., et al. 2018, ApJL, 861, L3
Cañameras, R., Nesvadba, N. P. H., Guery, D., et al. 2015, A&A, 581, A105
Cantalupo, S., Arrigoni-Battaia, F., Prochaska, J. X., Hennawi, J. F., & Madau, P. 2014, Natur, 506, 63
Carilli, C. L., & Walter, F. 2013, ARA&A, 51, 105
Daddi, E., Dannerbauer, H., Liu, D., et al. 2015, A&A, 577, A46
Daddi, E., Elbaz, D., Walter, F., et al. 2010, ApJL, 714, L118
Danese, L., de Zotti, G., & di Tullio, G. 1980, A&A, 82, 322
Dannerbauer, H., Harrington, K., Díaz-Sánchez, A., et al. 2019, AJ, 158, 34
Dannerbauer, H., Lehnert, M. D., Emonts, B., et al. 2017, A&A, 608, A48
Decarli, R., Arrigoni-Battaia, F., Hennawi, J. F., et al. 2021, A&A, 645, L3
Emonts, B. H. C., Cai, Z., Prochaska, J. X., Li, Q., & Lehnert, M. D. 2019, ApJ, 887, 86
Emonts, B. H. C., Lehnert, M. D., Dannerbauer, H., et al. 2018, MNRAS, 477, L60
Emonts, B. H. C., Lehnert, M. D., Villar-Martín, M., et al. 2016, Sci, 354, 1128
Emonts, B. H. C., Norris, R. P., Feain, I., et al. 2014, MNRAS, 438, 2898
Evrard, A. E., Bialek, J., Busha, M., et al. 2008, ApJ, 672, 122
Genzel, R., Baker, A. J., Tacconi, L. J., et al. 2003, ApJ, 584, 633
Genzel, R., Tacconi, L. J., Gracia-Carpio, J., et al. 2010, MNRAS, 407, 2091
Ginolfi, M., Maiolino, R., Nagao, T., et al. 2017, MNRAS, 468, 3468
Gómez-Guijarro, C., Riechers, D. A., Pavesi, R., et al. 2019, ApJ, 872, 117
Goto, T., & Toft, S. 2015, A&A, 579, A17
Harrington, K. C., Yun, M. S., Cybulski, R., et al. 2016, MNRAS, 458, 4383
Harris, A. I., Baker, A. J., Zonak, S. G., et al. 2010, ApJ, 723, 1139
Hennawi, J. F., Prochaska, J. X., Cantalupo, S., & Arrigoni-Battaia, F. 2015, Sci, 348, 779
Ivison, R. J., Smail, I., Le Borgne, J. F., et al. 1998, MNRAS, 298, 583
Kennicutt, R. C., Jr. 1998, ARA&A, 36, 189
Kirkpatrick, A., Sharon, C., Keller, E., & Pope, A. 2019, ApJ, 879, 41
Koekemoer, A. M., Fruchter, A. S., Hook, R. N., & Hack, W. 2003, in The 2002 HST Calibration Workshop : Hubble after the Installation of the ACS and the NICMOS Cooling System, ed. S. Arribas, A. Koekemoer, & B. Whitmore (Baltimore, MD: Space Telescope Science Institute), 337
Li, Q., Cai, Z., Prochaska, J. X., et al. 2019, ApJ, 875, 130
Magdis, G. E., Rigopoulou, D., Hopwood, R., et al. 2014, ApJ, 796, 63
Miley, G. K., Overzier, R. A., Zirm, A. W., et al. 2006, ApJL, 650, L29
Miller, T. B., Chapman, S. C., Aravena, M., et al. 2018, Natur, 556, 469
Munari, E., Biviano, A., Borgani, S., Murante, G., & Fabjan, D. 2013, MNRAS, 430, 2638
Nesvadba, N. P. H., Lehnert, M. D., Eisenhauer, F., et al. 2006, ApJ, 650, 693
Oteo, I., Ivison, R. J., Dunne, L., et al. 2018, ApJ, 856, 72

Pentericci, L., Roettgering, H. J. A., Miley, G. K., Carilli, C. L., & McCarthy, P. 1997, A&A, 326, 580
Reid, M. J., Schneps, M. H., Moran, J. M., et al. 1988, ApJ, 330, 809
Riechers, D. A. 2013, Natur, 502, 459
Riechers, D. A., Boogaard, L. A., Decarli, R., et al. 2020, ApJL, 896, L21
Ruel, J., Bazin, G., Bayliss, M., et al. 2014, ApJ, 792, 45
Saro, A., Mohr, J. J., Bazin, G., & Dolag, K. 2013, ApJ, 772, 47
Sharon, C. E., Riechers, D. A., Hodge, J., et al. 2016, ApJ, 827, 18
Solomon, P. M., Downes, D., & Radford, S. J. E. 1992, ApJL, 387, L55
Strandet, M. L., Weiss, A., De Breuck, C., et al. 2017, ApJL, 842, L15
Ueda, J., Iono, D., Yun, M. S., et al. 2014, ApJS, 214, 1
Wagg, J., & Kanekar, N. 2012, ApJL, 751, L24
Wang, T., Elbaz, D., Daddi, E., et al. 2016, ApJ, 828, 56
White, M., Cohn, J. D., & Smit, R. 2010, MNRAS, 408, 1818
White, M., Myers, A. D., Ross, N. P., et al. 2012, MNRAS, 424, 933
Wilkinson, A., Almaini, O., Chen, C.-C., et al. 2017, MNRAS, 464, 1380
Yang, C., Omont, A., Beelen, A., et al. 2017, A&A, 608, A144
Yang, Y., Decarli, R., Dannerbauer, H., et al. 2012, ApJ, 744, 178
Yang, Y., Walter, F., Decarli, R., et al. 2014, ApJ, 784, 171
Yang, Y., Zabludoff, A., Eisenstein, D., & Davé, R. 2010, ApJ, 719, 1654